INSTRUMENTATION FOR STUDIES OF ELECTRON EMISSION AND CHARGING FROM INSULATORS

C.D. Thomson
Physics Department, Utah State University
SER 250 UMC 4415
Logan, UT, USA 84322-4415
Phone: 435.797.2936
Fax: 436.797.2492
E-mail: JR.Dennison@usu.edu

V. Zavyalov, J.R. Dennison
Physics Department, Utah State University

Abstract

Making measurements of electron emission properties of insulators is difficult since insulators can charge either negatively or positively under charge particle bombardment. In addition, high incident energies or high fluences can result in modification of a material's conductivity, bulk and surface charge profile, structural makeup through bond breaking and defect creation, and emission properties. We discuss here some of the charging difficulties associated with making insulator-yield measurements and review the methods used in previous studies of electron emission from insulators. We present work undertaken by our group to make consistent and accurate measurements of the electron/ion yield properties for numerous thin-film and thick insulator materials using innovative instrumentation and techniques. We also summarize some of the necessary instrumentation developed for this purpose including fast-response, low-noise, high-sensitivity ammeters; signal isolation and interface to standard computer data acquisition apparatus using opto-isolation, sample-and-hold, and boxcar integration techniques; computer control, automation and timing using Labview software; a multiple sample carousel; a pulsed, compact, low-energy, charge neutralization electron flood gun; and pulsed visible and UV light neutralization sources. This work is supported through funding from the NASA Space Environments and Effects Program and the NASA Graduate Research Fellowship Program.

Introduction: Absolute Electron Yield Measurements for Spacecraft Charging

A key contributor to the spacecraft charging process is electron-induced secondary electron (SE) emission. SE's are low-energy (<50 eV) electrons that are emitted from a material resulting from incident electron, ion, or photon bombardment. In order to predict the extent of spacecraft differential charging in modeling codes it is mandatory to accurately determine *absolute* SE yield parameters that include the maximum electron yield, δ_{max} and its corresponding energy, E_{max} as well as the first and second crossover energies, E_1 and E_2, at which the material transitions between positive and negative charging. Previous experimental studies have determined values for these parameters for some materials, but most measurements were taken in poor-quality vacuums, and were susceptible to contamination effects. Furthermore, most electron yield data has not been carefully referenced to accurate standards (Holliday, 1957). Furthermore, past

attempts to calibrate detector systems have only been partially successful. In all reviewed cases, second order corrections corresponding to absorption and scattering (within the detector apparatus) were neglected. Consequently, existing electron yield data that have been corrected against previous standards may be relatively correct, but the absolute accuracy remains uncertain.

A primary focus of the research at Utah State University (USU) has been the development of instrumentation and methods for measuring absolute total, SE, and back scattered electron (excited electrons with energies >50 eV, termed BSE) yields of numerous conductor and insulator materials to incorporate into the NASA/SEE Charge Collector material database (Dennison, 2002). For the last few years, measurements have been made on various conductor samples using a DC-measurement system that has involved continuous electron, ion, and photon sources along with sensitive slow-response ammeters used to measure electron currents. Improvements at USU described here include data acquisition in an ultra-high vacuum (UHV) environment for surface contamination control, and the utilization of a fully enclosing hemispherical grid detection system that has been calibrated (both through calculation and measurement) to account for detector losses. These corrections ensure the accuracy of our absolute yield measurements. A review of our recently extended capabilities to make insulator-yield measurements using pulsed electron-beam sources, in addition to optically isolated, fast-response sensitive electronics and various charge-neutralization techniques is given. Both the DC- and pulsed-yield setups are fully automated such that multiple measurements can be made in a short turn-around time. A complete description of the DC-system setup as well as the pulsed-system setup, along with additional insulator-yield and charging data is available in other works (Thomson, 2004; Nickles, 2002; Dennison, 2002).

This paper reports basic concepts, instrumentation, calibration and test results of both our DC- and pulsed- electron beam system to measure accurate SE and BSE yields of both insulators and conductors. Finally, validation of the pulsed-measurement system in comparison to the DC-measurement system will be shown along with pulsed-yield data on an anodized Al2219 alloy.

Overview of Insulators and Conductor Yield Measurements

Historically, SE and BSE yields have been measured by either using a sample biasing scheme (to either attract or repel SE's) or by using a retarding field grid (biased between 0 V and -50 V) detector. Of these two approaches, the grid/detector scheme is considered to be more accurate, although technically more complicated since all electron current entering or leaving the measuring apparatus needs to be accounted for (Nickles, 2002; Seiler, 1983). This often requires the utilization of several sensitive ammeters that can float independently. It has been well established that small changes in absolute magnitude of yield coefficients can have substantial effects on spacecraft potentials [Davies, 1997; Chang, 2000]. Hence, it is essential that our experimental investigations provide calibration of absolute electron yield measurements, with a target of ~5% accuracy.

Such measurements on conductors are straightforward since a constant electron current source can be utilized and DC-currents coming off of the sample can be measured using standard picoammeters. Additionally, by grounding the conductor sample, any charge that leaves or is

absorbed into the material can be immediately neutralized to ground. Electron yield measurements on dielectrics are more difficult to make than on conductors, since any charge that is deposited in the material cannot easily be dissipated. During measurements of electron emission properties of insulators, charge builds up near the sample surface because of low bulk and surface conductivity and lack of charge dissipation. The resulting sample potentials that develop can affect incident electron landing energies, and produce energy shifts of the emitted electrons, and consequently lead to significant errors in the measured SE and BSE yield measurements. To control insulator charging, pulsed-electron beams and neutralization sources are implemented.

An important phenomenon that limits the incident-electron pulse width and frequency practical for SE yield measurements on insulators is a surface potential buildup during the primary electron pulse. This potential is proportional to the total charge deposited on the insulator surface, which is directly related to the electron pulse duration and electron beam intensity, that is to total electron fluence. This implies a primary limitation on the pulse-measurement system design with regards to the speed and sensitivity of the ammeters used for detecting electron yield currents. Other limitations arise from the necessity to monitor low-level currents from several sources that are biased over a range of zero to hundreds of volts. The DC measurement scheme built at USU has proven to be one of the most accurate and versatile systems for the metrological absolute measurements of the emission properties of conducting materials. Based on this previous experience for conductive materials, a similar pulse measurement scheme for the insulating materials has been developed and tested.

General Experimental Setup

A simple schematic of the measurement setup is shown in Fig. 1. The sample is enclosed in the hemispherical detection apparatus, and an incident electron (or ion) beam enters into the assembly through a tubular aperture in the back of the detector housing. Sensitive ammeters are tied independently to the electron collector, biasing grid, sample, and sample stage to account for all incident and emitted electron current. The retarding grid can be biased negatively (or positively) to reject or pass electrons excited from the sample. Potentials on the suppression grid are controlled using a Keithley 230 voltage supply controlled via GPIB interfacing by a computer for both DC and pulsed-yield setups. The electron collector always remains at a +50 V bias (supplied by a standard power supply with the DC-yield setup and with batteries for the pulsed-yield setup) with respect to the retarding grid both to ensure that all electrons passing through the grid reach the collector, and also to ensure that any SE's emitted from the collector are returned to the collector. Total and BSE yields are directly measured by applying a 0 V or -50 V bias to the retarding grid, and then by taking the ratio of the collector current over the total incident current. The total incident current can be determined in three ways: i) by directly monitoring the electron gun emission current; ii) by measuring the total gun current using a Faraday cup; iii) or by simply summing the sample, grid, collector and stage currents. All three methods have been shown to produce results for the total incident current consistent to ~3 %; the third method is more expedient, and was therefore implemented most often.

Details of the USU surface analysis chamber are given in Dennison (2003). All measurements are performed in an UHV chamber pumped with turbomolecular and ionization

pumps to pressures ranging from 10^{-10} to 10^{-8} Torr (determined using ion gauges), depending on the sample data set. Ion gauges are turned off during measurements as they emit stray electron and ion current (fractions of nanoamperes) into the chamber. Hence, the gauges act as an agent for positive insulator charging, and also affect the yield measurements by introducing stray currents.

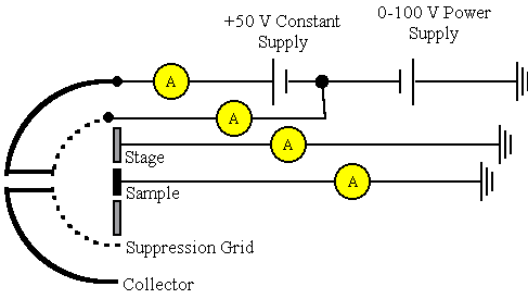

Figure 1. Basic schematic for DC- and pulsed- yield measurements. The incident electron beam enters through the detector aperture tube. Collector, retarding grid, sample, and stage currents are measured to calculate electron yields.

Two electron guns are available for making yield measurements: a low-energy gun (STAIB EK-5-S, energy range 50eV to 5 keV with pulsing capabilities from 1μs to continuous emission), and a high-energy gun (Kimball ERG-21, energy ranging from 4 keV to 30 keV, pulsing from 10 ns to continuous emission). Both guns provide beam currents ranging from 10-100 nA, with beam spot diameters ranging from 0.8 to 2 mm depending on the energy. Samples are placed on an 11-sample carousel that can be swung around to face the electron sources (Dennison, 2003). Thin-film conductor foils and insulator films are glued to 10.0 ± 0.1 mm diameter Oxygen Free High Conductivity (OFHC) copper cylinders using a UHV adhesive containing fine silver powder to provide electrical contact between the films and substrate.

DC-Yield Measurement System

Using the detector setup described above, electron yields are measured using the DC-setup shown in Fig. 2. Yields are then calculated as ratios of the emitted current to the total incident current. For total yield measurements, the grid bias is set to 0 V, and are calculated in terms of the collector, sample, stage and grid currents. BSE yields are measured and calculated in a similar manner, with the grid potential at -50 V. Yield equations are then

$$\sigma = \frac{I_{Collector}}{I_{Incident}} = \frac{I_{Collector}}{I_{Collector} + I_{Sample} + I_{Stage} + I_{Grid}(0V)} \quad \text{and}$$

$$\eta = \frac{I_{Collector}}{I_{Collector} + I_{Sample} + I_{Stage} + I_{Grid}(-50V)}$$

Finally, SE yields are calculated as the difference between the BSE and SE yields as $\delta = \sigma - \eta$.

To achieve our goal of 5% accuracy in yield measurements, a retarding field energy analyzer and direct current measurement using electrometers have been used by us and other investigators (Nickles, 2002), rather than more precise or sensitive energy analyzers or detectors. However, accurate absolute yield measurements using such grid analyzers require corrections for scattering off the grids and other detector surfaces and for other geometrical factors. Spherical or hemispherical retarding grids are most common, as their radial electrostatic fields provide better energy resolution. Corrections for spherical grids that fully surround the sample are much simpler to determine than those for hemispherical grids (Sternglass, 1953; Jonker, 1951). However, we have used hemispherical grids to facilitate use of a sample carousel for increased sample throughput (Nickles, 2002).

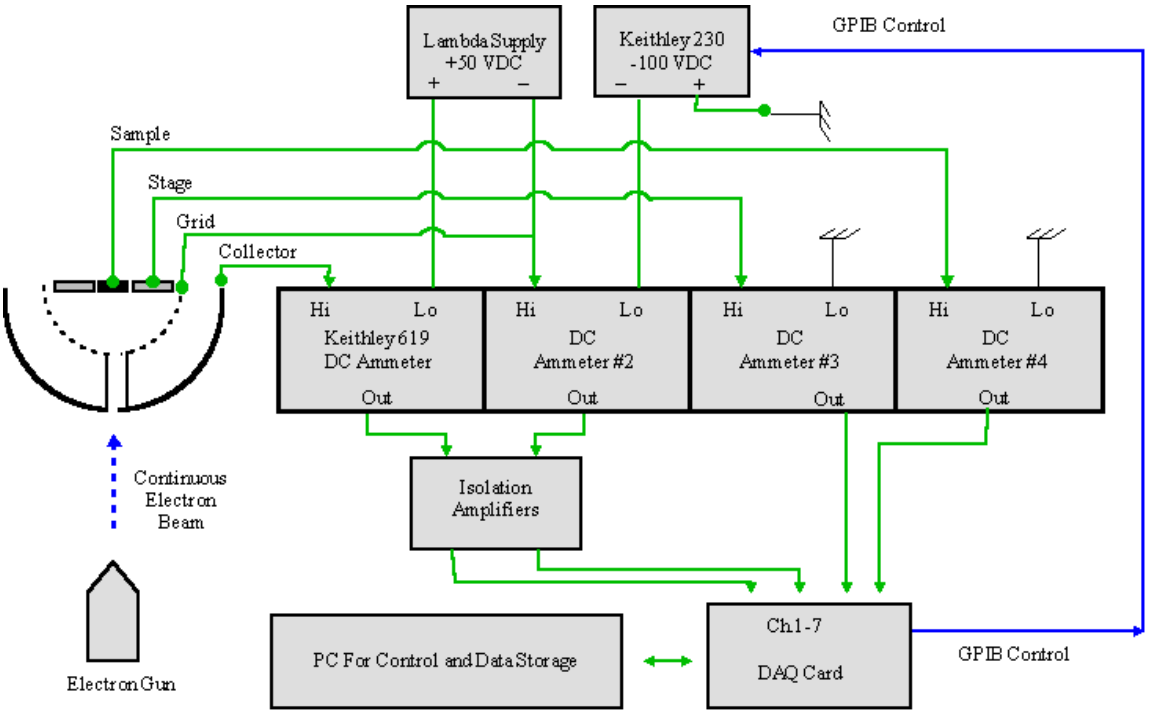

Figure 2. DC-yield measurement block diagram for conductors.

We have arrived at a consistent set of correction factors with <5% uncertainty for the various types of measurements performed using the USU detector. Determination of the correction factor values was based on consideration of: (i) numerous calibration measurements; (ii) detailed numerical modeling of the grid corrections for our apparatus; and (iii) comparison with previous yield measurements by other investigators, where available. Validation experiments and comparison with prior studies of SE, BSE and ion yields were made for polycrystalline Au samples, because Au has been studied extensively and is relatively free of contamination effects due to its inert nature. Uncertainties in the calibration measurements and modeling of the grid corrections were all at about the 5% level, consistent with our target objective for accuracy of absolute yield measurements.

A complete discussion of grid correction calculations for our detector for total yield, BSE yield, SE yield, ion yield, and photoyield are presented elsewhere (Nickles, 2002; Thomson, 2004). The largest grid correction is the opacity of the grids, accounting for ~75% of the full correction factor. Smaller "blocking" corrections of ~5%, based solely on the geometry of the detector, account for electrons not reaching the collector due to less than 10% of the solid half-sphere not subtended by the grids. This includes electrons lost out the electron beam incidence aperture and electrons that hit the beam tube or other detector surfaces before reaching the collector. The third largest correction is for BSE reflected from the collector. Coating the collector with colloidal graphite that has a particularly low BS yield of 0.07 [Sternglass, 1953] is a standard method used to reduce this correction; in our case it is reduced to a ~4% correction. Note that essentially all SE leaving the collector are returned to the collector because the retarding grid is always held at –50 V with respect to the collector. Also note that many high emission angle BSE have trajectories that return them to the collector before reaching the retarding grid. Additional smaller correction terms involve multiple SE or BSE scatter.

Overview of the Pulsed-Yield Setup

Although a completely independent measuring circuit was used for pulsed-yield measurements (see Fig. 3) the basic block diagram is much the same as for the DC-measurements (see Fig. 2). However, optically isolated fast (1-2 μs rise time) sensitive/low noise (10^7 V/A / 100 pA noise level) ammeters were developed to measure electron emission bursts that were emitted from the sample and detecting surfaces, and are described in more detail below. Careful shielding and grounding schemes were used to eliminate electromagnetic and power-line noise to the signals.

For pulsed measurements, a digital TTL signal from the computer DAQ card was used to activate a timing circuit that delivered a simultaneous trigger to both a pulse generator and signal-integrator circuits. Upon receiving this trigger, the pulse generator delivered a 5 μs square-wave firing pulse (100 ns rise time) to the electron gun. Total and BSE current pulses from the sample, stage, retarding grid, and collector were measured with the fast-response ammeter circuits described below. Typical emitted pulses are shown in Fig. 4 for the sample and collector. These pulses were integrated using either the integrator circuits or by storing the waveforms to a 500 MHz LeCroy digital storage oscilloscope and then exporting the data to a computer for further analysis. Both data acquisition and analysis were fully automated using Labview 5.0. After signal integration was performed, yields were calculated similar to the DC setup by taking the ratios of the emitted charge to the total incident charge as:

$$\sigma = \frac{Q_{Collector}}{Q_{Incident}} = \frac{\int I_{Collector}\,dt}{\int I_{Collector}\,dt + \int I_{Sample}\,dt + \int I_{Stage}\,dt + \int I_{Grid}(0V)\,dt} \quad ,$$

$$\eta = \frac{Q_{Collector}(>50V)}{Q_{Incident}} = \frac{\int I_{Collector}\,dt}{\int I_{Collector}(>50V)\,dt + \int I_{Sample}\,dt + \int I_{Stage}\,dt + \int I_{Grid}(-50V)\,dt} \quad \text{and}$$

$$\delta = \sigma - \eta$$

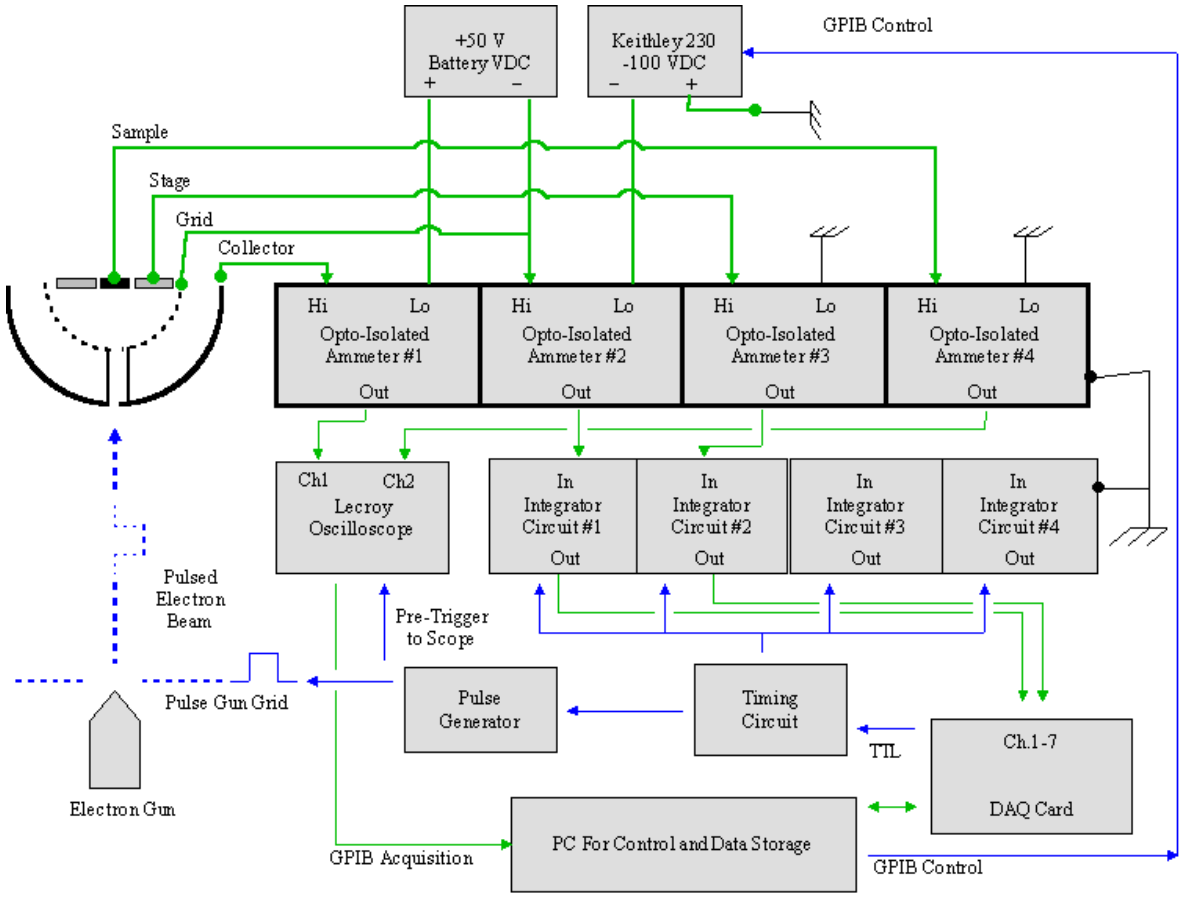

Figure 3. Pulsed-yield measurement block diagram for insulators.

Details of the Pulsing Circuitry

Most commercially available picoammeters have a low frequency bandwidth and are designed for current measurements with respect to the ground, and cannot be used for floating current measurements. To protect a data acquisition system from high floating voltages, and to avoid galvanic coupling between measurement and data acquisition circuitry, isolation amplifiers are needed as an interface between the input current detectors and the output voltage signals of the data acquisition system. Isolation amplifiers also reject large common-mode signals appearing at the input, and dampen ground loops since the inputs and outputs are floating relative to each other. For low current, low-noise, and wide frequency bandwidth floating current measurements, optically coupled isolation amplifiers are favored against modular devices using transformer-coupled modulation-demodulation. Optically coupled isolation amplifiers have the advantage of smaller size, wider bandwidth and integrated circuit reliability. Also, they use a DC-analog modulation technique that steers clear of problems associated with electromagnetic interference and coupling that most inductively coupled isolation amplifiers exhibit.

The circuit schematic of the opto-isolated ammeter (Fig 5) is composed of three stages. The first stage is a current-to-voltage converter that is a classic transimpedance amplifier based on a

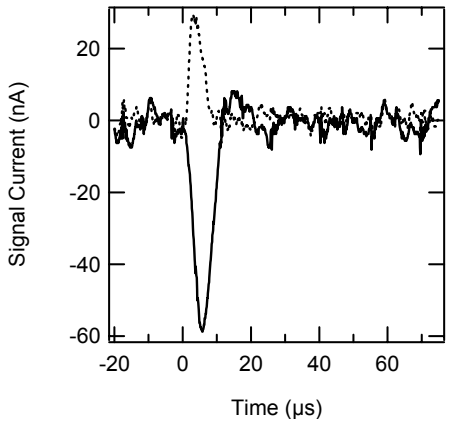

Figure 4. Measured sample (dot) and collector (solid) electron 5 μs, 50 nA pulses on Au at 800 eV. Similar pulsed signals were obtained for stage and grid surfaces. Delayed rise and fall times were caused by system capacitance and ammeter response times.

low-noise and low-leakage current OPA602BP DIFIT op amp. As a rule most of the noise is induced on the first transimpedance stage of the ammeter so that optimal design of this stage is crucial for the overall performance of the ammeter. The feedback resistor, R_f was selected as a compromise between sensitivity, low noise performance, and highest possible speed to fulfill the electron impulse magnitude and duration limitations discussed above. The signal-to noise (SNR) ratio of the transimpedance stage is SNR = 10 log(I_{in} R_f^2/ $2eB_f(1+R_f/R_s)^2$) where I_{in} is the input current (1-100 nA), R_f is the feedback resistance, B_f is the frequency bandwidth, and R_s is an effective current source resistance. It is seen that the higher the feedback resistance, the better the SNR. However, source C_s, feedback C_f, and input op amp, C_{in} capacitances slow down the time response of the transimpedance amplifier with time constants $\tau=R_fC_{in,s,f}$ and significantly limit the optimal value of the feedback resistor R_f. It is found that the ammeter frequency response for feedback resistor values R_f <100 MΩ is mostly defined by the input capacitance that is an order of 3-7 pF for most of the available op amps. Taking this into account, the optimal value for the feedback resistor was selected in a range of 10-100 kΩ that allows us to achieve good sensitivity in the nanoampere current region, and low-noise performance at the level of 2-5 $pA/Hz^{1/2}$, and a high frequency bandwidth of 200-400 kHz.

The second stage is a high linearity bipolar isolation amplifier with a gain of A_{op}=2 or 10, selectable by a switch on the front panel of the ammeter. A wide bandwidth (DC to >1 MHz) HCNR200 analog optocoupler, with a low nonlinearity of 0.01% and a stable transfer gain ($K_3=I_{pd1}/I_{pd2}$) was chosen for this stage. The stage transfers the voltage signal from the first transimpedance stage to the third amplifying stage through optical coupling. The optocouplers allow a large potential difference (~2.6 kV) between a common input ground and an output ground. Optical coupling is achieved through a light emitting diode (LED) with two matching photodiodes (PD1 and PD2) detecting optical signals from the same LED. Because of the unipolar nature of the LED, two optocouplers are combined together to provide bipolar optical coupling (see Fig. 5). Relatively small values of R_{in} and R_{11} (values recommended by the manufacture are typically >100 kΩ) are chosen to provide the optocouplers' wide frequency

band of ~1 MHz, given that the input and output time constants are defined primarily by the photodiode capacitance of C_{pd}~22 pF as $\tau_{in}=C_{pd1}R_{in}$ and $\tau_{out}=C_{pd2}R_{11}$.

The third gain stage is composed of a standard inverting voltage amplifier, U7 with a gain of A=100. To provide amplification in a wide frequency bandwidth without any distortion of the signal detected by the first transimpedance stage, a low cost OP37GP op amp with a 63 Mhz frequency bandwidth was chosen for this stage as well as for optocoupler stages of the ammeter.

An overall output voltage of the 3 stage opto-isolated ammeter is thus defined as $V_{out}= T A_{op} A= I_{in}R_f A_{op} A= I_{in}R_f K_3(R_{11}/R_{in})A \sim I_{in}R_f AR_{11}/R_{in}$ where T is the transimpedance stage gain, A_{op} is the opto-isolation amplifier gain, and A is the output stage gain. The overall gain may be selected by switches S1 (gain T) and S2 (gain A_{op}) on the ammeter front panel for a combined range of $2x10^6 - 1x10^8$ V/A (K_3=1 and A=100). The feedback potentiometer, R8, is used to set an overall amplifier gain to calibrate the ammeter, where $G=TA_{op}A$.

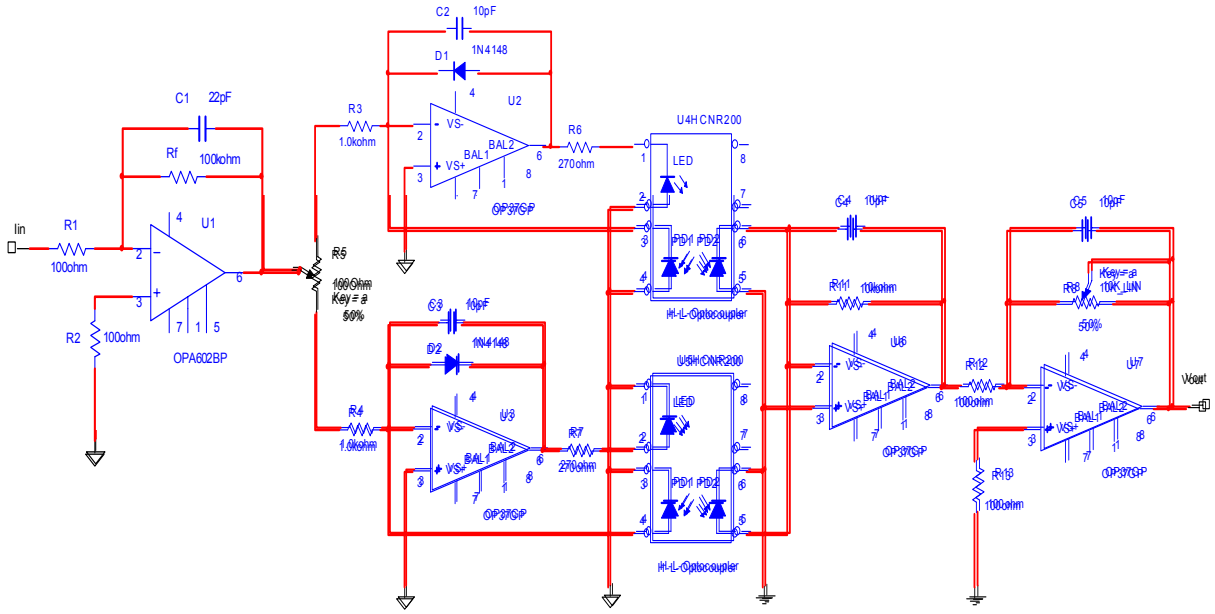

Figure 5. Circuit diagram of opto-isolated ammeter.

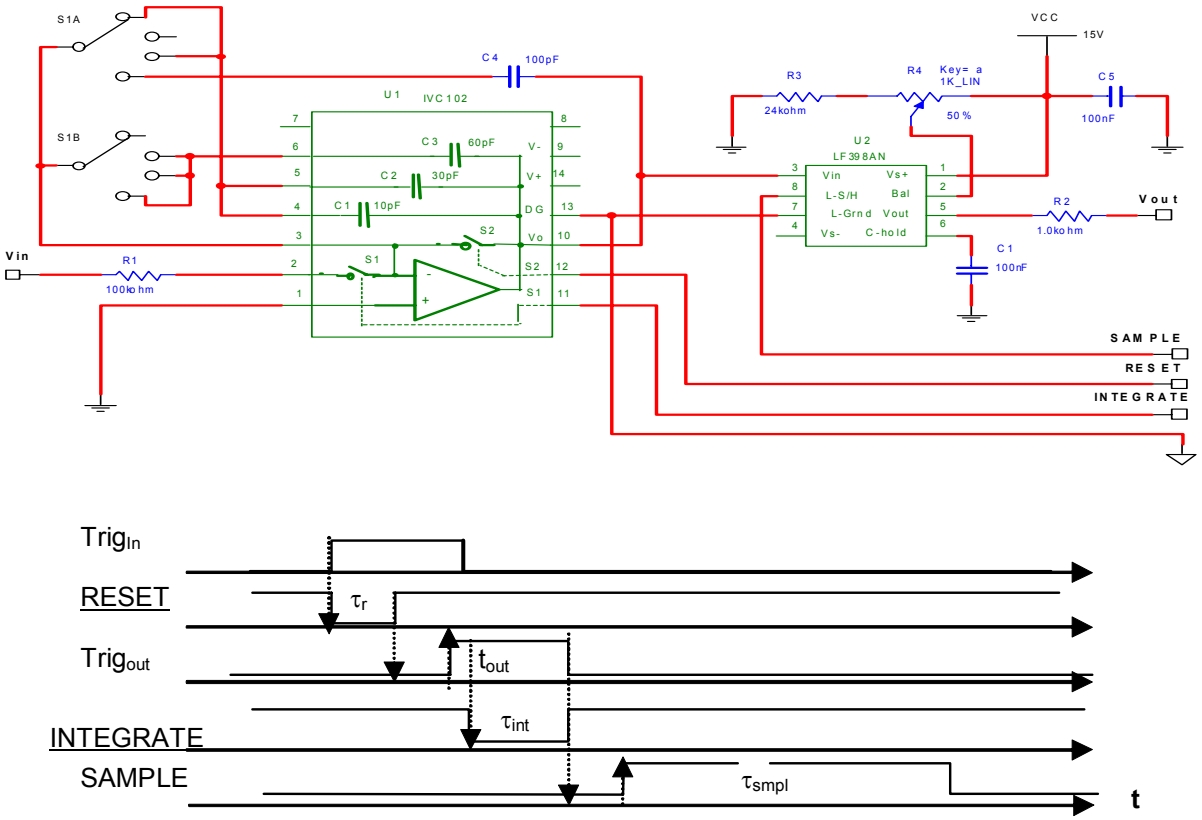

Figure 6. Circuit diagram of the switched integrator and timing diagram of the sample-and-hold circuitry.

To convert a short impulse voltage signal from the ammeter to the DC output voltage, which can then be recorded by the computer through a data acquisition board, a switched integrator is used. A circuit diagram of the integrator and sample-and-hold circuit is shown in Fig. 6. For the integrating stage, an IVC102 precision integrating amplifier was chosen. This amplifier is based on a low-bias current FET op amp with integrating capacitors (C_1-C_3), and low leakage FET switches (S_1 and S_2)—all integrated on the same chip. Since the complete circuit is on a single chip, the IVC102 eliminates many of the problems commonly encountered in discrete designs, such as leakage current errors, stray capacitance interference, voltage offset drift, and noise pickup. High quality metal-oxide internal capacitors with excellent dielectric characteristics provide high temperature stability and low nonlinearity of ~0.005% that is especially important for short integration times. TTL/CMOS-compatible timing inputs (switches S1 and S2) control the integration period, as well as hold and reset functions to set the effective transimpedance gain and reset (discharge) the integrator capacitor. The transfer function of the integrator is:

$$V_{out} = \frac{1}{T}\int_{t1}^{t2} V_{in}dt = \frac{1}{T}\int_{t1}^{t2} I_{in}(t)R_fGdt = \frac{R_fG}{T}\int_{t1}^{t2} I_{in}(t)dt$$

where $V_{in} = I_{in}(t)R_fG$ and V_{out} are input and output voltages of the integrator, $I_{in}(t)$ is a measured current at the ammeter input, R_f is the feedback resistor of the ammeter first transimpedance

stage, $\Delta t=t_2-t_1$ is an integration time and $T=R_{int}C_{int}$ is the integrator time constant. The last integral is simply the charge measured for the time duration, Δt, so that the final expression is:

$$V_{out} = \frac{Q}{T} R_f G = (\Delta t/T)\ (I_{in} R_f G)$$

Note that the integration time, Δt, should be longer than or equal to the current impulse duration. The integration time and the integrator time constant may be set independently over a range of 4-100 μsec.

Finally, to control the proper operation of the switched integrator and sample-and-hold circuit, a simple digital pattern generator (not shown) is used. This generator creates TTL level digital signals to control the RESET, INTEGRATE, and SAMPLE switches at a rate controlled by the trigger signal $Trig_{In}$ from a computer. A timing diagram of these control impulses is shown in Fig. 6.

Neutralization Techniques

Methods for insulator charge neutralization included a low-energy electron flood gun source (energies <1 eV) mounted adjacent to the sample (see Fig. 7) in the sample block, separated (center of gun aperture to center of sample) by 11 mm. The gun extraction grid potential was switched from suppression to emission mode for a few seconds between each incident electron pulse to neutralize positive surface charging as described above. This process was self regulating in that once the positive insulator was neutralized, the low energy electrons were no longer attracted to the surface, and a steady state current corresponding to a near-zero surface potential was achieved. The amount of flood gun current drawn to the sample was dependent on the gun's filament current and extraction potential as well as the sample potential. To test the effectiveness of the flood gun, a gold sample was placed next to the gun. Sample current was monitored as the sample was biased to positive potentials ranging from 0-50 V for three different extraction potentials, while maintaining a constant filament current of 1.3 A as shown in Fig. 8. Each data set was fitted with an asymptotically approaching exponential function. At a sample potential of 0 V, the current drawn from the flood gun varied from 6-75 nA, depending on extraction potential. This indicated that operating the flood gun for 1 s would deliver 4-5 orders of magnitude more electron fluence to the sample surface than a typical 5 μs, 50 nA incident electron pulse containing ~10^6 electrons/pulse.

The effectiveness of the electron flood gun method remained questionable for eliminating negative surface charge or charge beneath the insulator surface. Either visible or UV light with energies of a fraction of the insulator bandgap (<10 eV) have been shown to stimulate photo-induced conductivity in materials such as Kapton™ and polyethylene, and thereby accelerate the discharging process (Bass, 1998; Levy, 1985). To assist in the neutralization of negative charge, a mercury-gas and tungsten-filament lamp were mounted next to a quartz view port with a focusing lens to irradiate the samples. Measured intensities of the focused beams at the sample faces were ~35 mW/cm^2. We found the electron flood gun to be the most effective tool for charge neutralization below 1 keV, based on yield-repeatability measurements. Preliminary discharging measurements on a chromic-anodized Al2219 alloy using the flood gun, mercury, and tungsten lamps are discussed elsewhere (Thomson, 2003).

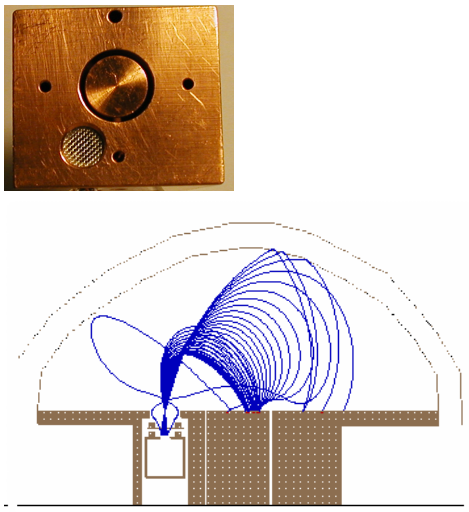

Figure 7. An electron flood gun sits adjacent to insulator samples and neutralizes positive surface charge. Top: a picture of the flood gun and sample. Bottom: a SIMION simulation of the flood gun inside the detector cavity next to a positively charged sample at +0.5 V and retarding grid at -1 V

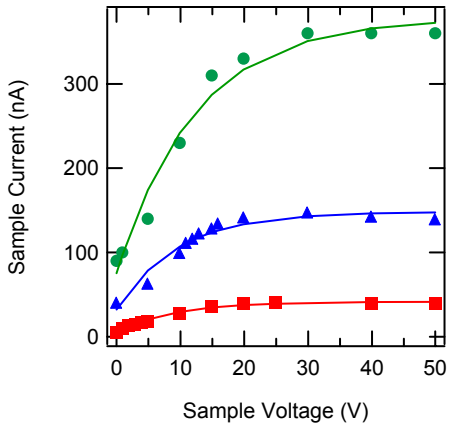

Figure 8. Flood gun current to a biased Au sample. I_{Fil}=1.3 A for all data; only the gun extraction potential is varied from 4 V (●), 3 V (▲), and 2 V (■). Sample current ranges from 5.5 nA to 75 nA at a 0 V sample potential, and from 42 nA to 380 nA at saturation.

Pulsed-Yield Measurements

The pulsed-yield setup was first tested on a conducting titanium sample to compare results directly to the DC-yield setup. The offsets and linearity of the four pulse ammeters were first calibrated using an oscilloscope (average of 100 traces of the pulse ammeters) and an accurate DC-ammeter over the range of 0-100 nA to an uncertainty of <0.5 nA using the low-energy electron gun in DC-mode (as a constant current source) at 400 eV. Next, operating the gun in single-pulsed mode at 5 μs pulse duration, 50 nA pulse magnitude, and at 400 eV the total collector charge was measured and calculated for each of the three ammeter amplification

settings ($2\cdot10^6$ V/A, $1\cdot10^7$ V/A, and $2\cdot10^7$ V/A) for all ammeters, and results were compared for consistency. Variations between ammeter settings $1\cdot10^7$ V/A and $2\cdot10^7$ V/A were less than the uncertainty of repeated measurements on an individual setting, <10%. However, variations between the $2\cdot10^6$ V/A setting and the other two settings ranged between 20-50% most likely due to the poor signal-to-noise-ratio of the lower gain setting.

Integrator circuits were tested in comparison to charge-integration calculations using the trapezoidal-rule. This was done for two different time duration/integration time constant settings: $\Delta t/T$=21.5/15.5 µs and $\Delta t/T$=12.5/9.0 µs for both $1\cdot10^7$ V/A and $2\cdot10^7$ V/A ammeter settings. Error between integrator circuit and computational integrations were ~10% for all settings, however, results were slightly better when using an ammeter amplification of $2\cdot10^7$ V/A with $\Delta t/T$= 21.5/15.5 µs settings. Variations in the integration results were attributed to small current DC offsets in the pulsed signals that were later adjusted for in Labview software data acquisitioning.

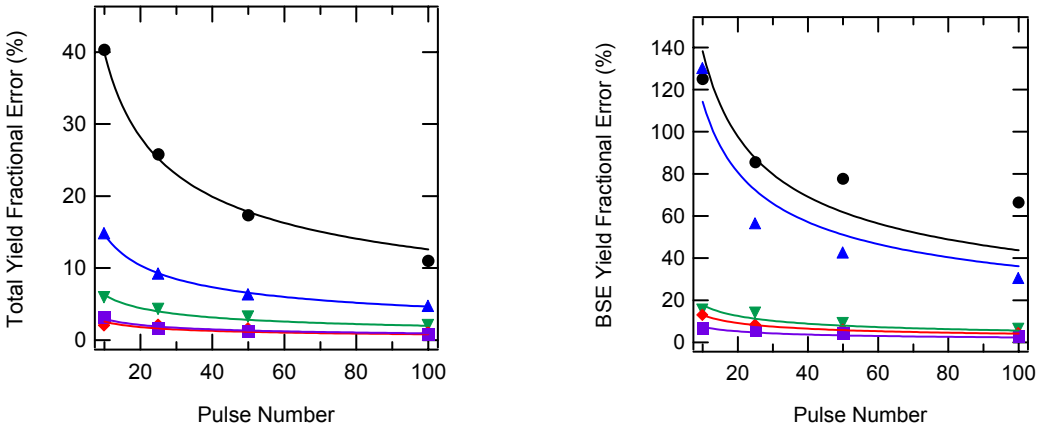

Figure 9. Fractional error as a function of pulse current magnitude and number of pulses for total yields (top) and BSE yields (bottom) using the low energy STAIB gun at 400 eV on conducting Ti at 10 nA (●), 25 nA (▲), 50 nA (▼), 75 nA (♦), and 100 nA (■) impulse magnitudes. Fits vary as the inverse of the root of the number of pulses.

Repeated insulator measurements at a given beam energy were averaged to decrease the electron yield uncertainty, but came at the expense of both greater data acquisition time (since the sample must be flooded between incident pulses) and increased sample radiation exposure. In order to balance measurement uncertainty with sample irradiation exposure, error diagnostics for the pulsed-yield system were performed by taking 100 single-pulse total and BSE yield measurements on conducting titanium at different 5 µs impulse magnitudes of 10 nA, 25 nA, 50 nA, 75 nA, and 100 nA (as measured by the collector) at a beam energy of 400 eV. Results for the percent fractional error for both total and BSE yields are shown in Fig. 9, and depended both on the signal amplitude and on the number of pulses/measurement. Data are fitted with

$$\%FE(N) = \frac{100}{\sqrt{N}}\left(\frac{YLD_{Stdev}}{YLD_{Mean}}\right)$$

where N is the number of pulses/yield measurement, YLD_{Stdev} is the yield standard deviation and YLD_{Mean} is the average yield value. Data was generally taken using ten pulses/measurement at 50 nA impulse magnitude such that the percent fractional errors were 5% and 20% for SE and BSE yields, respectively.

The absolute accuracy of the pulsed-yield measurements was tested on a titanium sample and compared to DC-yield results with discrepancies <5%. As can be seen in Fig. 10, the two approaches are quite comparable for total, SE, and BSE yields. Additionally, a pulsed SE spectrum was taken at beam energy 400 eV on titanium as shown in Fig. 11.

Finally, to demonstrate the pulsed setup on an insulator, a yield curve was taken on insulating anodized Al 2219 alloy as shown in Fig. 12 along with the Feldman semi-empirical fit used in the SEE Charge Collector Knowledge Base (Dennison, 2002). The flood gun was used after each electron beam pulse to neutralize the sample. Estimates for the maximum yield were δ_{max}=3.0±0.1 at E_{max}=300±50 eV, and the first and second crossover energies were E_1=50±10 eV and E_2=1400±100 eV. Further data on this and other insulator samples is provided in other conference proceedings (Thomson, 2003).

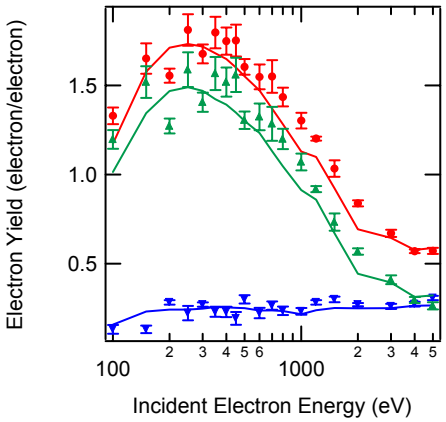

Figure 10. Comparison of pulsed total (●), SE (▲), and BSE (▼) yields with DC (solid lines) yields for Ti. Each data point is the mean of 10 pulses (standard error as bars), of time duration 5 µs and magnitude 50 nA.

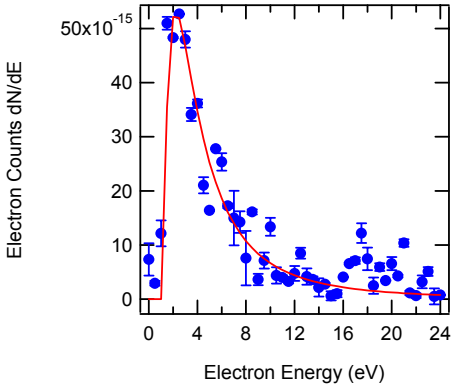

Figure 11. Pulsed-yield SE spectra on Ti at 400 eV. Data is fit with the Chung and Everhart model. Each data point is the mean of 10 pulses (standard error as bars), of time duration 5 µs and magnitude 50 nA.

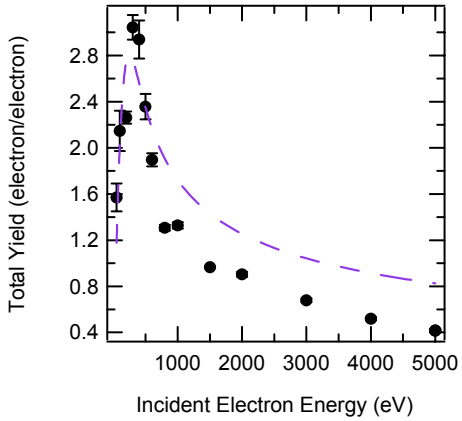

Figure 12. Pulsed-total yields (5 µs pulses with amplitudes 50 nA, each data point is 10 pulses) for insulating anodized Al2219 fitted with a Feldman Model.

Summary and Conclusions

The measurement of absolute SE, BSE, and total yields of both conductor and insulator materials provides important parameters for the NASA/SEE's Charge Collector material database. At USU, we have performed careful calibration of our detector setup to make accurate SE yields on conductors and insulator materials with absolute uncertainties of <5 %. We have also developed fast-response, optically isolated electron detection equipment that is synchronized with the pulsing of electron guns, integrator circuits, and computer data acquisition. Neutralization techniques such as electron flooding and UV sources have also been implemented. The absolute yields for a titanium conductor sample were measured, and have been shown to produce consistent results using both the pulsed-yield and DC-yield setup. Finally, pulsed-yield measurements on an anodized Al2219 aluminum alloy insulating sample have been demonstrated without significant charging distortions.

Acknowledgments

The work presented was supported in part by the NASA Space Environments and Effects (SEE) Program and a NASA Graduate Fellowship through Marshall Spaceflight Center. Samples were supplied by the Materials, Processes, and Manufacturing Department at NASA Marshall Space Flight Center, and Sheldahl, Inc.

References

1. A.D. Bass, P. Cloutier, and L. Sanche, "Measurements of charge accumulation induced by monochromatic low-energy electrons at the surface of insulating samples," J. Appl. Phys. 84 (5), 2740-2748 (1998).

2. Davies, R.E and J.R. Dennison, "Evolution of Secondary Electron Emission Characteristics of Spacecraft Surfaces," J. Spacecraft and Rockets, 34, 571-574 (1997).

3. J.R. Dennison, W.Y. Chang, N. Nickles, J. Kite, C.D. Thomson, Jodie Corbridge, and Carl Ellsworth, "Final Report Part III: Materials Reports," NASA Space Environments and Effects Program Grant, "Electronic Properties of Materials with Application to Spacecraft Charging," September 2002; Available in electronic format through NASA SEE as part of the SEE Charge Collector Knowledgebase.

4. J.R. Dennison, C.D. Thomson, J. Kite, V. Zavyalov, Jodie Corbridge, "Materials characterization at Utah State University: facilities and knowledgebase of electronic properties of materials applicable to spacecraft charging," Proceedings of the 8th Spacecraft Charging Technology Conference, October 20-24, 2003, Huntsville, Alabama.

5. J.E. Holliday, and E. J. Sternglass, 1957, "Backscattering of 5-20 keV electrons from insulators and metals," J. Appl. Phys. 28, 1189-1193.

6. J.H.L. Jonker, "The angular-distribution of the secondary electrons of nickel," Philips Res. Rep. 6, 372-387 (1951).

7. L. Levy, D. Sarrail, and J.M. Siguier, "Conductivity and secondary electron emission properties of dielectrics as required by NASCAP," Proceedings of the Third European Symposium on Spacecraft Materials in Space Environment, Noordwijk, The Netherlands, October 1-4, 1985.

8. Neal E. Nickles, The Role of Bandgap in the Secondary Electron Emission of Small Bandgap Semiconductors: Studies of Graphitic Carbon, Ph.D. dissertation, Utah State University, 2002.

9. H. Seiler, "Secondary electron emission in the scanning electron microscope," J. Appl. Phys. 54 (11), R1-R18 (1983).

10. E. J. Sternglass, An Experimental Investigation of Electron Back-Scattered and Secondary Electron Emission From Solids, Ph.D. thesis, Cornell University, 1953.

11. C.D. Thomson, V. Zavyalov, J.R. Dennison, Jodie Corbridge, "Electron Emission Properties of Insulator Materials Pertinent to the International Space Station," Proceedings of the 8th Spacecraft Charging Technology Conference, October 20-24, 2003, Huntsville, Alabama.

12. C.D. Thomson, Measurements of the Secondary Electron Emission Properties of Insulators, Ph.D. dissertation, Utah State University, 2004.